Minimally invasive molecular delivery into the brain using optical modulation of vascular permeability

Myunghwan Choi[a], Taeyun Ku[b], Kyuha Chong[b], Jonghee Yoon[a], and Chulhee Choi[a,b,c,d,1]

[a]Department of Bio and Brain Engineering, [b]Graduate School of Medical Science and Engineering, [c]KI for the BioCentury, and [d]Optical BioImaging Center, Korea Advanced Institute of Science and Technology, Daejeon 305-701, Korea

Edited by Hee-Sup Shin, Korea Institute of Science and Technology, Seoul, Republic of Korea, and approved April 26, 2011 (received for review December 15, 2010)

Systemic delivery of bioactive molecules in the CNS is hampered by the blood–brain barrier, which has bottlenecked noninvasive physiological study of the brain and the development of CNS drugs. Here we report that irradiation with an ultrashort pulsed laser to the blood vessel wall induces transient leakage of blood plasma without compromising vascular integrity. By combining this method with a systemic injection, we delivered target molecules in various tissues, including the brain cortex. This tool allows minimally invasive local delivery of chemical probes, nanoparticles, and viral vectors into the brain cortex. Furthermore, we demonstrated astrocyte-mediated vasodilation in vivo without opening the skull, using this method to load a calcium indicator in conjunction with label-free photoactivation of astrocytes.

femtosecond pulsed laser | laser tissue interaction | molecular delivery | permeability

Microvascular endothelial cells in the brain are interconnected through complex tight junctions, forming a physiological barrier against endogenous and exogenous molecules (1). Becauee of this blood–brain barrier (BBB), nearly 100% of macromolecules and more than 98% of small molecules do not cross the blood vessel wall. Thus, exogenously introduced molecular probes are widely used in vivo to study the molecular physiology of the brain. Systemic delivery through the blood circulation would be a safe, effective, and desirable method of distributing molecular probes or drugs into the brain.

Various strategies have been proposed to circumvent the BBB. A transcranial approach invasively bypasses the BBB by drilling a hole in the head and injecting probes or drugs intracerebrally or intracerebroventricularly (2). At present, intracerebral injection is the gold standard for in vivo brain experiments; however, the invasiveness of opening the skull and inserting a pipette remains controversial (3, 4). A transnasal approach can noninvasively deliver molecular probes or drugs across the nasal mucosal barrier, but is limited to lipid-soluble small molecules (5). Another approach is to chemically modify therapeutic agents so that they can traverse the BBB effectively by enhancing lipid solubility, lowering molecular weight, or taking advantage of an endogenous transporter-mediated process. Various BBB disruption methods also have been proposed, including intracarotid arterial infusion of vasoactive agents and local ultrasonic irradiation with i.v. microbubble injection (6). However, no method allows the noninvasive and spatially specific delivery of large molecules into the brain.

Near-infrared femtosecond pulsed lasers have been widely used for in vivo imaging because of their deep tissue penetration, reduced scattering, and localized nonlinear absorption. These properties also have enabled noninvasive optical modulation of live cells and tissues with subcellular resolution, including the generation of intracellular calcium, dissection of intracellular organelles, transient plasma membrane permeabilization, induction of arterial contraction, and disruption of blood flow (7–12). In the present study, we explored the use of a near-infrared ultrashort pulsed laser for minimally invasive molecular delivery into the brain.

Results

Femtosecond Pulsed Laser Induces Local and Transient Vascular Permeability to Macromolecules with Minimal Invasiveness. To test the feasibility of optical delivery of macromolecules, we first examined whether femtosecond laser irradiation focused on a vessel wall induces vascular permeabilization in the brain. We used i.v. 2 MDa FITC-dextran, which does not leak in normal cortical vasculature, as the plasma indicator. The nonlinear optical nature of the pulsed laser enables specific targeting of subsurface vasculature without compromising the superficial regions; thus, we used a murine thinned-skull window model to image the brain cortex with minimal invasiveness. We selected cortical veins after imaging the cortical vasculature. Arteries were excluded to avoid femtosecond laser-induced arterial contraction (12) that could potentially compromise neurovascular regulation, and capillaries were excluded because of their physical vulnerability (Fig. S1). After laser irradiation to the vessel wall, the targeted vessel wall displayed localized leakage of the blood plasma propagating to the nearby parenchyma (Fig. 1 *A* and *B*). This laser-induced extravasation exhibited an all-or-none response in a laser energy-dependent manner (Fig. S2). Blood vessels ranging from superficial pial veins to deep cortical venules were successfully targeted without perturbing superficial vasculature (Fig. S3). A regional time-series analysis demonstrated diffusion of the fluorescent probe into the surrounding region, followed by decreased fluorescence intensity at the core of the permeation, suggesting that the changes in vascular permeability might have been transient (Fig. 1*C*). Because red blood cells (RBCs) are not fluorescent, they appear as dark circular structures in the positively stained blood plasma. Occasionally, we observed transient clot formation in the luminal side around the irradiated region concurrent with disturbed blood flow (9 of 104 cases). However, this usually disappeared within several minutes, and blood flow recovered accordingly (Fig. S1). For a sustained period after laser irradiation, we detected no negative signals moving in the extravasated area, indicating that no significant RBCs leakage during laser-induced vascular permeability. We further validated this finding by injecting fluorescently stained RBCs before inducing extravasation (Fig. S4).

We next investigated the dependency of the laser-induced extravasation profile on vessel properties. To compare vascular parameters, we measured lumen diameter and blood flow, which were positively correlated in the brain (Fig. S5*A*; $n = 37$ in five animals). We analyzed the extravasated area and circularity of plasma extravasation at 1 min after laser irradiation. Notably, compared with large venules (lumen diameter >25 μm; $n = 9$), small venules (lumen diameter <25 μm; $n = 28$) exhibited sig-

Author contributions: M.C. and C.C. designed research; M.C., T.K., K.C., and J.Y. performed research; M.C., T.K., K.C., J.Y., and C.C. analyzed data; and M.C. and C.C. wrote the paper.

The authors declare no conflict of interest.

This article is a PNAS Direct Submission.

Freely available online through the PNAS open access option.

[1]To whom correspondence should be addressed. E-mail: cchoi@kaist.ac.kr.

This article contains supporting information online at www.pnas.org/lookup/suppl/doi:10.1073/pnas.1018790108/-/DCSupplemental.

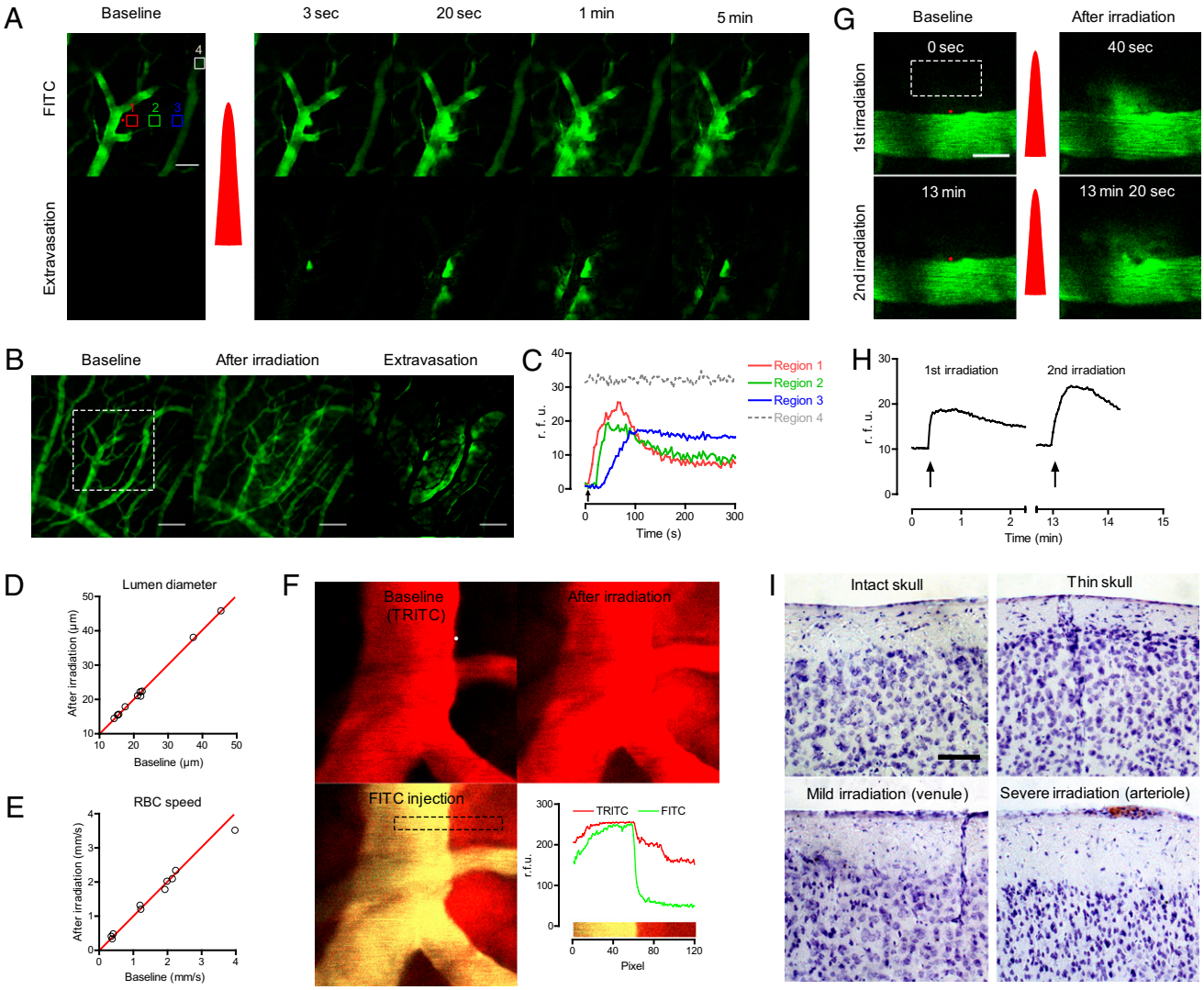

Fig. 1. Optical modulation of vascular permeability in the brain. (*A*) Time-series two-photon laser scanning microscopic images of a cortical vein in the brain. After i.v. injection of 2 MDa of FITC-dextran, the thinned-skull window was imaged with two-photon microscopy. A red dot indicates the position of laser irradiation, and the red pulse indicates laser irradiation. Extravasation images were acquired by subtracting the baseline image. (Scale bar: 50 μm.) (*B*) Z-projection images obtained at baseline and at 5 min after irradiation. A white rectangle indicates the region of interest in *A*. (Scale bar: 100 μm.) (*C*) Regional time kinetics of fluorescence. The regions are indicated by the boxes in *A* with the corresponding numbers and colors. rfu, relative fluorescence unit. (*D* and *E*) Lumen diameter and red blood cell speed were measured before and after inducing extravasation. Red lines show $y = x$, indicating no change. (*F*) Extravasation was induced (*Upper Right*) after measuring the baseline vascular structure using 70-kDa TRITC-dextran (*Upper Left*). After 10 min, 70-kDa FITC-dextran was injected to evaluate BBB integrity (*Lower Left*). (*Lower Right*) Distribution of the two fluorescent probes in the region indicated with a dashed rectangle. (*G* and *H*) Extravasation could be repeated by irradiating the laser at the same position. In *G*, the red dots indicate the region of laser irradiation, and the red pulses indicate laser irradiation. Arrows in *H* indicate the time of laser irradiation. (Scale bar: 20 μm.) (*I*) Nissl-stained brains with intact skull, thinned skull, mild laser irradiation targeted on a venule, and severe laser irradiation targeted on arteriole. The red region in the lower right panel indicates a blood clot caused by severe photodamage. (Scale bar: 50 μm.)

nificantly larger extravasation areas (Fig. S5*B*). Consistent with the positive correlation between lumen diameter and blood flow, slower blood flow tended to be correlated with larger extravasation area, albeit nonsignificantly (Fig. S5*C*). Venules with a smaller diameter or slower blood flow were positively correlated with higher circularity of extravasation (Fig. S5 *D* and *E*). Accordingly, the extravasation area was positively correlated with the circularity of extravasation (Fig. S5*F*).

We also measured the volume of plasma leakage during laser-induced extravasation. After injecting quantum dots along with 2 MDa of FITC-dextran i.v., we evoked laser-induced extravasation in cortical venules and counted the number of leaked quantum dots in the brain parenchyma. We measured the concentration of quantum dots in the blood plasma from the blood sample, to convert the number of quantum dots to plasma leakage volume. The estimated plasma leakage was 1.3 ± 0.2 pL (n = 8). Because the conventional pipette-based bulk loading method for staining the brain requires ~0.4 pL of a dye solution (13), we considered the volume of plasma leakage by our method to be adequate for use in molecular delivery into the brain.

We next examined the effect of the laser-induced extravasation on the targeted blood vessel. We monitored changes in lumen diameter, blood flow, and BBB integrity to quantitatively investigate structural and functional changes due to laser irradiation. To compare lumen diameter and blood flow, we acquired baseline data for vascular structure and RBC speed and then repeated the same measurements after 10 min of induced extravasation. We detected no noticeable change in either para-

meter by laser-induced extravasation (Fig. 1 *D* and *E*). To examine BBB integrity, we used the leakage of a 70-kDa dextran-conjugated dye as a marker of a disrupted BBB (14). First, we induced extravasation with 70-kDa dextran conjugated with a red-colored TRITC and waited for 10 min. Then we i.v. injected the dextran conjugated with a green-colored FITC to check for restoration of BBB integrity. Simultaneous imaging of the two dyes clearly showed that the later-introduced FITC-dextran resided only in the lumen, whereas the TRITC-dextran remained in both the lumen and extravasated region (Fig. 1*F*). This finding lends further support to the transiency of laser-induced vascular permeabilization. Having confirmed structural and functional integrity, we then tested the repeatability of the laser-induced extravasation. By applying laser irradiation at the same position with the same or higher power, we could induce extravasation repeatedly (Fig. 1 *G* and *H*).

We performed postmortem and functional analyses to further evaluate the potential damage to surrounding parenchyma. First, we performed Nissl staining at 3 h after inducing extravasation to assess the acute effect on cell death. The Nissl staining demonstrated no significant neuronal damage by skull thinning or mild laser irradiation targeted to a venule, which induced transient extravasation of a 2-MDa dextran-conjugated dye (Fig. 1*I*). To assess the delayed effect on cell death and immune response, we performed Nissl staining and immunohistochemistry on the astrocyte and microglial activation markers GFAP and Iba-1 at 2 d after inducing extravasation (3). We found no noticeable cell death or immune response in the region (Fig. S6). Finally, we monitored spontaneous glial calcium activity during laser-induced extravasation to evaluate any potential modification to cellular functional activity by leaked plasma. After plasma leakage, astrocytes showed a transient activation in the spontaneous calcium signal, but those cells restored baseline activity within 10 min (Fig. S7). Collectively, these data suggest that although laser-induced vascular permeabilization can transiently perturb the functional activity of nearby cells, these effects are reversible and do not involve cell death or immune response.

Minimally Invasive Molecular Delivery of Bioactive Macromolecules to the Brain Parenchyma. Given the ubiquitous presence of blood vessels, we hypothesized that laser-induced vascular permeabilization with i.v. administration of target molecules could be applied for molecular delivery. To test this hypothesis, we first used Hoechst 33342 nuclear staining dye. Because of its limited penetration into cell layers, i.v. administered Hoechst is confined to the lumen or vascular wall without affecting parenchymal tissues where the BBB remains intact (15). In a thinned-skull window model, we i.v. injected 2 MDa of FITC-dextran and Hoechst simultaneously. In the brain, both dyes were confined to the lumen of the cortical vasculature. After laser irradiation to the vessel wall, the dyes propagated to surrounding parenchymal tissue with different diffusion kinetics (Fig. 2 *A* and *C*). At approximately 5 min after irradiation, the accumulation of the Hoechst signal was visible as ring-shaped structures, which became solid circles with brighter fluorescence, indicating progressive nuclear binding (Fig. 2 *A* and *B*). By subtracting the FITC-dextran image from the Hoechst image, we could selectively visualize the nuclei stained with Hoechst (Fig. 2*D*).

We then used sulforhodamine 101 (SR101), which specifically stains astrocytes. SR101 is also used for angiography, suggesting that it does not leak in healthy vasculature (16). Extravasation was induced after i.v. injection of 2 MDa of FITC-dextran as a plasma marker and SR101 (Fig. 2*E*). After 2 h, we observed stained astrocytes, as well as the vasculature around the irradiated region. By subtracting the FITC-dextran image from the SR101 image, we could selectively visualize the stained astrocytes (Fig. 2*F*). A region in the other hemisphere showed no noticeable staining with SR101, suggesting that the astrocyte staining was actively mediated by the laser-induced extravasation. Furthermore, we confirmed that laser-induced extravasation is feasible using quantum dots (Q21021MP; Invitrogen) and tetramethylrhodamine (TAMRA)-conjugated magnetic oxide nanoparticles (MiONs), suggesting wide applicability of this technique (Fig. S8).

Next, we used adenovirus vectors encoding GFP to test the feasibility of laser-induced extravasation as a gene-delivery tool in the brain. The adenovirus has a hydrodynamic size of ∼100 nm and does not cross the BBB, limiting its use in CNS gene delivery

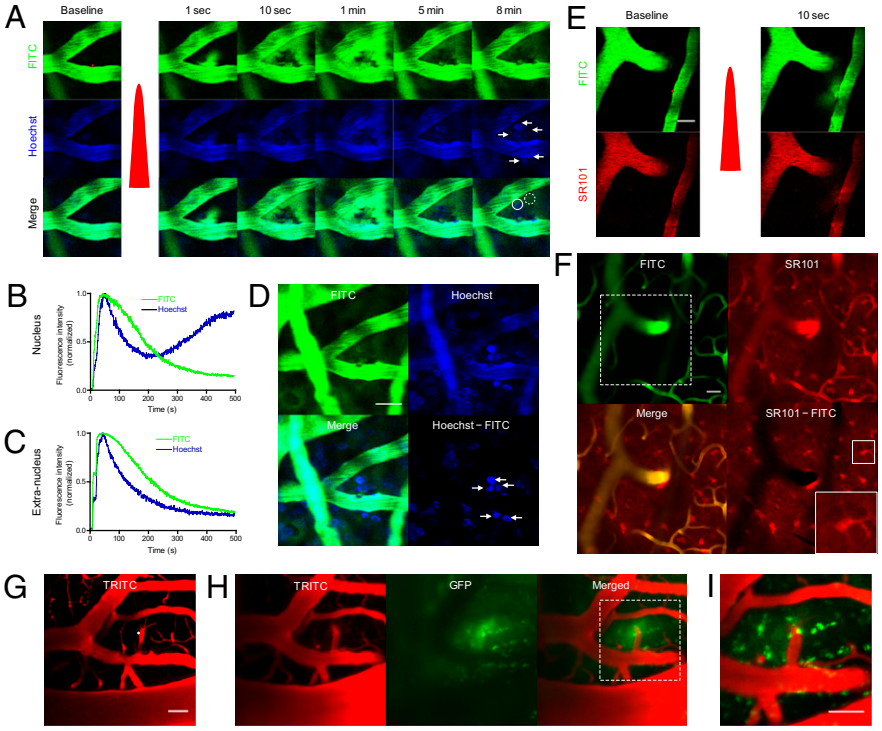

Fig. 2. Minimally invasive bulk loading of probes and adenovirus in the brain. (*A*) Time-course images of bolus dye loading and nuclear staining. Both Hoechst 33342 and 2 MDa FITC-dextran were injected i.v., and extravasation was induced. The red dot indicates the irradiated region. White arrows denote the stained nucleus. (*B* and *C*) Time course of intranuclear (solid line circle in *A*) and extranuclear (dashed line circle in *A*) FITC-dextran and Hoechst loading. (*D*) Local nuclear staining in the brain cortex. The image was obtained 30 min after induction of extravasation. Note the clear nuclear staining near the irradiated region (arrows). (Scale bar: 20 μm.) (*E*) Bolus astrocyte-specific dye loading with laser-induced vascular permeabilization. Both FITC-dextran and SR101 were injected i.v., and extravasation was induced. The red dot indicates the region of laser irradiation; the red pulse indicates laser irradiation. (Scale bar: 20 μm.) (*F*) Staining of astrocytes in the brain by imaging the same region at 2 h after extravasation. The white dashed box indicates the imaged region in *E*. White boxes in the lower right image show an enlarged, stained astrocyte. (Scale bar: 50 μm.) (*G*) Adenoviral gene delivery with laser-induced vascular permeabilization. Here 70-kDa rhodamine-dextran and GFP-adenovirus were injected i.v., and extravasation was induced by laser irradiation at the white dot. (Scale bar: 20 μm.) (*H*) Adenoviral infection. At 1 d after extravasation, the vasculature and GFP were imaged at the same region. (Scale bar: 20 μm.) (*I*) A magnified view of the white dotted box in *H*. (Scale bar: 50 μm.)

(17). After the skull-thinning surgery, we injected the plasma indicator rhodamine-dextran to identify the target venules. Considering its short plasma half-life of ~2 min, adenovirus was injected via an i.v. catheter about 5–10 s before induction of extravasation. The time interval of 5–10 s was determined experimentally by measuring the mean arrival time to the brain after injection of the dextran-conjugated FITC. To further increase the delivery efficiency, we induced multiple sequences of extravasations (two or three) by irradiating the same spot repeatedly. After 1 d, the same region was navigated by the vasculature pattern and imaged for vessel structure and GFP expression. The vasculature showed no noticeable change in structure or blood flow. Strong green fluorescence was detected in multiple cells only around the targeted region, indicating successful infection by the GFP-adenovirus (Fig. 2 *G–I*).

We next used a functional calcium indicator, Oregon Green BAPTA1-AM (OGB-1:00 AM), to test the applicability of laser-induced extravasation to the functional study of neurons and astrocytes. Because calcium indicators do not cross the BBB, transcranial delivery of a calcium indicator is the current standard for studying the functional dynamics of neuronal and glial networks in the brain. Counterstaining of astrocytes with SR101 is widely used, because calcium indicators stain both astrocytes and neurons (18). Because SR101 is highly stable in the blood, we used i.v.-injected SR101 to guide the vascular wall and stain astrocytes when extravasated. Due to a high level of esterases in the blood, acetoxymethyl (AM)-conjugated dyes have a relatively short plasma half-life (19). To increase the efficacy of molecular delivery, OGB-1:00 AM was injected via an intravascular catheter, and extravasation was induced 5–10 s after bolus injection. After 2 h, cellular staining of the calcium dye and astrocyte indicator was clearly visible around the irradiated region (Fig. 3*A*). The SR101 stained a larger area (300–400 μm diameter) compared with the calcium dye (150–200 μm diameter), presumably due to better diffusion kinetics. Consistent with previous studies using the conventional transcranial loading method, the calcium indicator stained both neurons and astrocytes (20). Neurons could be readily distinguished in the merged image by selecting cells stained only by the calcium dye after astrocyte counterstaining. We could detect spontaneous calcium activity in the stained neurons and astrocytes. In agreement with previous studies using the transcranial loading method, astrocytes demonstrated slow calcium dynamics on the minute time scale, and neurons exhibited infrequent, short-duration calcium transients (20) (Fig. 3*B*).

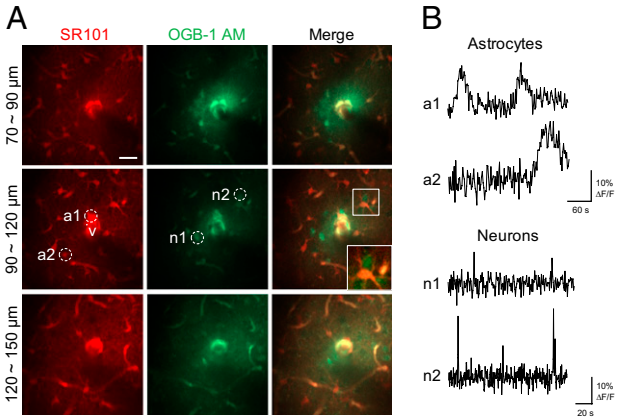

Fig. 3. Simultaneous bulk loading of a functional calcium indicator and an astrocyte marker in the brain using laser-induced vascular permeabilization. (*A*) Z-projected images of the brain stained with a calcium indicator (OGB-1:00 AM) and an astrocyte marker (SR101). Images were obtained at 2 h after delivery. The white dot indicates the region of laser irradiation. V indicates the targeted penetrating venule. White boxes show magnified views of stained cells. Imaging depths from the surface are indicated. (Scale bar: 20 μm.) (*B*) Spontaneous astrocytic and neuronal calcium activity. Images were obtained at 2 Hz in the region indicated by the dotted circles in *A*.

Tight spatial and temporal coupling of brain activity with local blood flow, so-called "neurovascular coupling," is a hallmark of brain function and is widely used for functional brain imaging (21). The pivotal role of astrocyte activity in neurovascular coupling is well known but has been demonstrated only in highly invasive preparations, such as ex vivo tissue cultures and an open-skull window model. We attempted to demonstrate the in vivo role of astrocytes in regulating neurovascular coupling with minimal invasiveness using the thinned-skull window model. After the skull thinning surgery, we injected rhodamine-dextran to select a target region in which an arteriole and venule were in close proximity. The calcium dye was injected via an i.v. catheter, and extravasation was induced at the surface venule (Fig. 4*A*). At 1 h after the laser-induced extravasation, we observed cells around the irradiated venule strongly stained by calcium dye (Fig. 4*B*). We observed stained cells at a cortical depth of 0–50 μm, where neurons are absent (18). These cells demonstrated typical astrocytic morphology and consistent baseline calcium signals, suggesting that intact cells were functionally stained.

To further validate functional loading of the calcium indicator, we selectively stimulated positively stained cells using a recently developed protocol with a label-free nonlinear optical technique (12). We selected a target astrocyte based on high baseline Ca^{2+} fluorescence, astrocyte-like morphology, and slow spontaneous Ca^{2+} dynamics. After laser stimulation, the targeted cell and surrounding cells showed synchronous increases in Ca^{2+} signals. Astrocytic endfeet sheathing the nearby arteriole also exhibited synchronous calcium activation, followed by vasodilation (Fig. 4 *C–F*).

Laser-Induced Extravasation Is Ubiquitously Applicable. We evaluated the feasibility of femtosecond laser-induced vascular permeabilization on tissues outside the CNS. We tested various optically accessible tissues, including the meninges, skull, striated muscle, and ear. The meningeal vasculature was visualized using a thinned-skull window, and the skull was imaged after the scalp wqas removed. A dorsal skinfold chamber model was used for striated muscle. For all types of tissues studied, femtosecond laser irradiation onto the vessel wall induced localized and transient leakage of 2 MDa of FITC-dextran, suggesting the versatility of laser-induced vascular permeabilization in a variety of tissues (Fig. 5).

Discussion

We have demonstrated that femtosecond pulsed laser irradiation induces transient and reversible permeabilization of the targeted blood vessel wall, causing extravasation of plasma along with bioactive macromolecules. By combining this method with systemic injection, we could locally deliver molecular probes, nanoparticles, and adenovirus into the brain cortex. We confirmed the feasibility of this method in various other tissues, including the meninges, ear, striated muscle, and bone. To demonstrate the feasibility of laser-induced extravasation for molecular delivery, we successfully stained the cortex with Hoechst, SR101, and a Ca^{2+} indicator. By combining optical delivery of a Ca^{2+} dye with label-free photoactivation of astrocytes, we examined the functional connectivity between perivascular astrocytes and cortical arterioles with intact skull and meninges.

The use of laser-induced vascular permeabilization as a molecular delivery tool has both benefits and drawbacks. The delivery site can be selected with subcellular resolution, and delivery is localized, allowing site-specific molecular delivery. The procedure is minimally invasive and repeatable, allowing increased efficiency of delivery by repeating extravasations or targeting multiple nearby blood vessels (Fig. S3*C*). Large molecules can be delivered into the brain where systemic delivery has been prevented by the BBB, thereby permitting the use of large chemical drugs, monoclonal antibodies, recombinant proteins, or gene therapies in the brain. The use of a femtosecond pulsed laser enabled intrinsic subsurface targeting; thus, we could stain the brain without opening the skull, which is necessary in con-

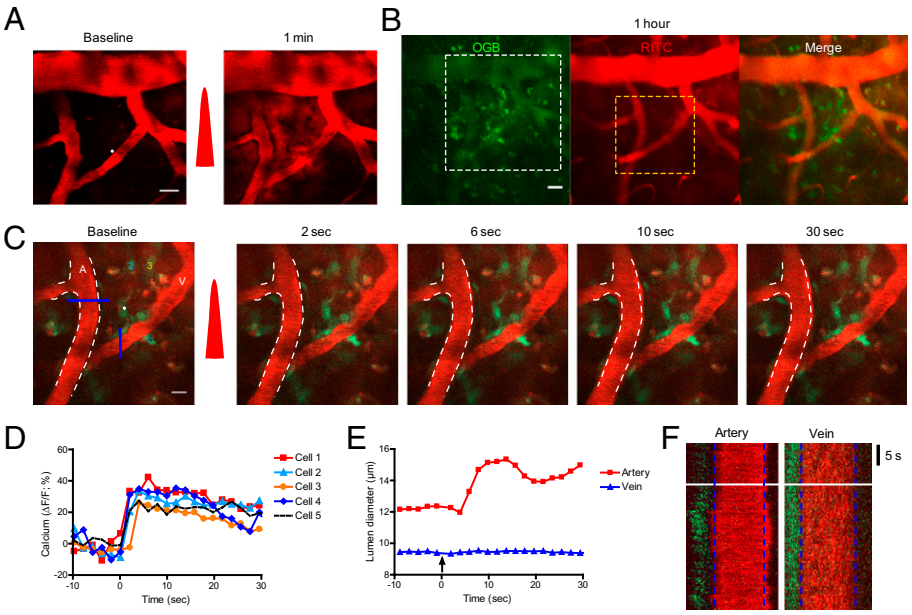

Fig. 4. Interrogation of astrocyte-mediated vasodilation in the brain. (*A*) Oregon Green Bapta-1:00 AM and rhodamine-dextran were injected i.v., and extravasation was induced via femtosecond laser irradiation. The white dot indicates the region of laser irradiation; the red pulse indicates laser irradiation. (Scale bar: 20 μm.) (*B*) Images were obtained at 1 h after extravasation. The white dotted box indicates the region of interest in *A*, and the yellow dotted box denotes the region of interest in *C*. (Scale bar: 20 μm.) (*C*) Time-series images of vasodilation by photoactivation of astrocytes. The white dot indicates the region of laser stimulation; the red pulse indicates laser irradiation. Note the calcium waves in the targeted and surrounding cells and subsequent vasodilation. The white dotted line demarcates the baseline lumen of the arteriole. The colored numbers indicate the cells used for calcium signal analysis in *D*. A, artery. V, vein. (Scale bar: 10 μm.) (*D*) Quantification of calcium signals in the cells and astrocyte endfeet around the artery. (*E* and *F*) Temporal kinetics of lumen diameter change in the artery and vein in *C*. The blue lines in *C* indicate the region used in *F*.

ventional brain staining for insertion of an injection pipette. Because skull opening causes microglial activation and intracranial pressure changes, and pipette insertion might further compromise tissue integrity, we propose the wide use of laser-induced extravasation for bulk loading of functional dyes in the brain (4). Drew et al. (22) demonstrated that a reinforced thinned-skull window is stable for months without causing brain inflammation. However, transcranial delivery is not possible using this model, because the skull is not opened. We expect that the use of the laser-induced molecular delivery method in this window model will facilitate minimally invasive chronic studies in the brain. However, the systemic injection procedure requires a large amount of target molecule due to dilution by blood plasma, and it is costly. Systemic injections of high dye or drug doses might carry potential risks of unwanted side effects. Moreover, the complex pharmacokinetics of a target molecule, such as accumulation in the liver, kidneys, or other tissues, could hinder precise estimation of molecular concentration in blood plasma. In addition, the current laser's tissue penetration depth is ∼1 mm, which limits target accessibility (23). Although we observed a correlation between vessel diameter and extravasation area, precise control of injection volume poses a challenge. Also, extravasated plasma may impair the integrity of the surrounding tissue (24). Although we observed no histopathological changes or irreversible functional disturbances by femtosecond pulsed laser irradiation in our study, caution must be taken to minimize laser-induced tissue damage.

Nishimura et al. (11) demonstrated that delivery of amplified low- repetition-rate (1 KHz) femtosecond laser pulses induces a targeted insult to individual subsurface cortical blood vessels, such as hemorrhage, intravascular clot formation, or extravasation. These authors reported irreversible blood clot formation in the target vasculature at 3 h after induction of extravasation. In the present study, we used an unamplified 80-MHz femtosecond laser, which is used widely for in vivo imaging. The use of an unamplified, high-repetition-rate pulsed laser could avoid the irreversible vascular damage or damage to surrounding tissue. Unlike amplified low-repetition-rate lasers, which depend primarily on photo-physical phenomena, the unamplified high-repetition-rate laser forms localized low-density plasma in the biological tissue (25). This generates photochemical effects with minimal thermal damage, such as the poration of plasma membranes (26) or generation of intracellular calcium waves, which presumably alter local vascular permeability. Although the exact in vivo mechanism for this is unclear, we suggest that the different mechanism of action resulted in minimally invasive modulation of vascular permeability, which can be used as a molecular delivery tool in the CNS.

The development of new probes or drugs delivered by laser-induced vascular permeabilization should meet several criteria used to select dyes. First, a dye should not be leaky in the healthy vasculature of the brain. Second, the dye should be stable in

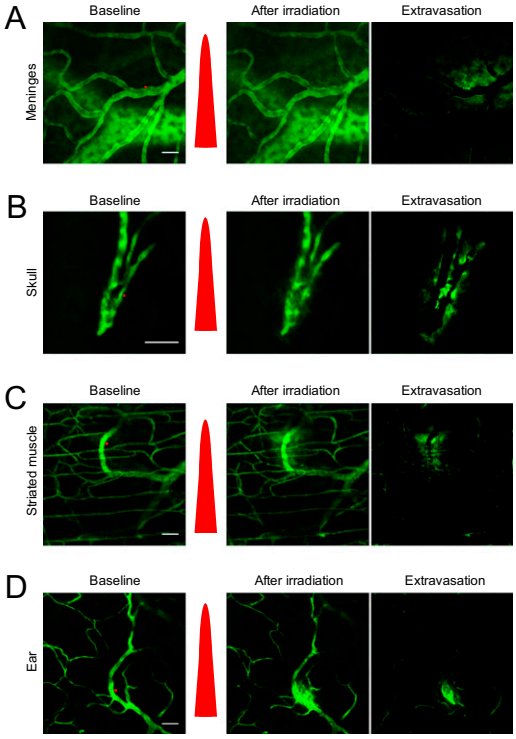

Fig. 5. Laser-induced vascular permeabilization in other vessel types. Red dots indicate the region of laser irradiation, and the red pulse indicates laser irradiation. (*A*) Meningeal vasculature. (*B*) Skull vasculature. (*C*) Striated muscle in the dorsal skin. (*D*) Ear. (Scale bar: 50 μm.)

the plasma and extravascular space. Vascular permeabilization should be performed quickly after i.v. administration for dyes with a short plasma half-life, such as adenoviruses or acetoxymethyl-conjugated dyes (19). Increasing plasma stability by chemical modification (e.g., adenovirus pegylation) also might be helpful (27). Finally, once extravasated, the dye must diffuse and reach the target, such as a nucleus or intracellular space.

The major obstacle to the use of laser-induced extravasation as a drug delivery system in the clinic is limited tissue accessibility. This problem can be ameliorated by introducing an endoscope near the target tissue; however, this might compromise the minimal invasiveness of the technique. Thus, the most promising candidate for clinical application of this technique is the retina, which is optically accessible. However, systemic drug delivery to the retina has proven problematic because of the blood–retinal barrier, which is similar to the BBB. A multiphoton fundus imaging system is currently under development (28), and we expect that clinical translation of this technique for retinal drug delivery will permit the use of large molecular drugs and provide a minimally invasive and spatially precise therapeutic modality.

Materials and Methods

Animal Model. The animal care and experimental procedures described herein were performed with approval from the Korea Advanced Institute for Science and Technology's Animal Care Committee. All experiments used 7- to 10-wk-old male ICR mice (Charles River Japan). An i.p. injection of ketamine-xylazine was used for anesthesia. Thinned-skull preparation was performed as described previously (4). After anesthesia, the scalp was removed and the skull was glued to a custom-designed metal plate (Namil Optical Components) using dental cement. Using a high-speed microdrill, a circular area of skull ~1–3 mm in diameter over the region of interest was thinned under a dissection microscope until a thin, smooth preparation was achieved. For the in vivo skull imaging experiments, the same procedures were used without the skull thinning. For the dorsal skinfold chamber model, we used a small dorsal skinfold chamber kit (SM100; APJ Trading) as described previously (29). In brief, mice were anesthetized, the dorsal skin was extended, and two mirror-image titanium frames were mounted. One layer of skin was excised, leaving the striated muscle of the opposite side intact, and then replaced with a glass coverslip mounted onto a frame. For in vivo ear imaging, mice were anesthetized, and the ear was glued to a glass slide and placed on a custom-designed mount.

Two-Photon Laser Scanning Microscopy. We performed two-photon laser scanning microscopy (LSM510; Carl Zeiss) with a femtosecond pulsed laser (Chameleon; Coherent) tuned to 800 nm and a water-immersion objective lens (20× with a 1.0 numerical aperture). The pulse width of the laser output was ~140 fs. For animal imaging after the skull-thinning surgery, a dye solution was injected i.v., and the mice were placed on a customized frame designed to minimize movement artifacts (Namil Optical Components). The average laser power used for imaging was <90 mW.

Laser Stimulation. The optical path and laser source for optical intervention were the same as those used for two-photon fluorescence imaging. For the laser-induced vascular permeabilization experiments, we selected target venules with a lumen diameter of 10–50 μm and a subsurface depth of up to 100 μm in a thinned-skull window model (Fig. S9). Vascular type was confirmed by measuring the direction of blood flow in the branching vessels. To target the vessel wall, a region outside the visualized luminal surface was selected for irradiation for a fixed duration of 1.6 ms. The average laser power was initially set at 300 mW and then increased up to 2000 mW until extravasation was observed. For the label-free photoactivation experiments, the cell body of the target astrocyte was irradiated for 160 μs. The average laser power was set initially at 300 mW and then increased up to 900 mW until the calcium signal wave was observed.

Image Processing. ImageJ and MATLAB were used for image processing and data quantification, respectively. The TurboReg or StackReg function was used to eliminate movement artifacts. Data are expressed as mean ± SEM.

Statistical Analysis. Statistical analyses were performed using Graph Pad Prism software. Data are expressed as mean ± SEM. Statistical differences were analyzed using the *t* test, where indicated. A P value < 0.05 was considered statistically significant.

ACKNOWLEDGMENTS. We thank Prof. Dal-Hee Min for providing the TAMRA-conjugated MiONs and Prof. Chan Park for advice on the histological analyses. This research was supported by Grant 2009K001282 from the Brain Research Center of the 21st Century Frontier Research Program funded by the Ministry of Education, Science, and Technology, Republic of Korea.

1. Brightman MW (1977) Morphology of blood–brain interfaces. *Exp Eye Res* 25(Suppl): 1–25.
2. Pardridge WM (2007) Blood–brain barrier delivery. *Drug Discov Today* 12:54–61.
3. Holtmaat A, et al. (2009) Long-term, high-resolution imaging in the mouse neocortex through a chronic cranial window. *Nat Protoc* 4:1128–1144.
4. Xu HT, Pan F, Yang G, Gan WB (2007) Choice of cranial window type for in vivo imaging affects dendritic spine turnover in the cortex. *Nat Neurosci* 10:549–551.
5. Hanson LR, Frey WH, 2nd (2008) Intranasal delivery bypasses the blood–brain barrier to target therapeutic agents to the central nervous system and treat neurodegenerative disease. *BMC Neurosci* 9(Suppl 3):S5.
6. McDannold N, Vykhodtseva N, Hynynen K (2008) Blood–brain barrier disruption induced by focused ultrasound and circulating preformed microbubbles appears to be characterized by the mechanical index. *Ultrasound Med Biol* 34:834–840.
7. Baker M (2010) Laser tricks without labels. *Nat Methods* 7:261–266.
8. Smith NI, et al. (2001) Generation of calcium waves in living cells by pulsed-laser–induced photodisruption. *Appl Phys Lett* 79:1208–1210.
9. Watanabe W, et al. (2004) Femtosecond laser disruption of subcellular organelles in a living cell. *Opt Express* 12:4203–4213.
10. Tirlapur UK, König K (2002) Targeted transfection by femtosecond laser. *Nature* 418: 290–291.
11. Nishimura N, et al. (2006) Targeted insult to subsurface cortical blood vessels using ultrashort laser pulses: Three models of stroke. *Nat Methods* 3:99–108.
12. Choi CJ, Belobraydich AR, Chan LL, Mathias PC, Cunningham BT (2010) Comparison of label-free biosensing in microplate, microfluidic, and spot-based affinity capture assays. *Anal Biochem* 405:1–10.
13. Stosiek C, Garaschuk O, Holthoff K, Konnerth A (2003) In vivo two-photon calcium imaging of neuronal networks. *Proc Natl Acad Sci USA* 100:7319–7324.
14. DiNapoli VA, Huber JD, Houser K, Li X, Rosen CL (2008) Early disruptions of the blood-brain barrier may contribute to exacerbated neuronal damage and prolonged functional recovery following stroke in aged rats. *Neurobiol Aging* 29:753–764.
15. Lyubimova NV, Coultas PG, Yuen K, Martin RF (2001) In vivo radioprotection of mouse brain endothelial cells by Hoechst 33342. *Br J Radiol* 74:77–82.
16. Zuluaga MF, et al. (2007) Synergies of VEGF inhibition and photodynamic therapy in the treatment of age-related macular degeneration. *Invest Ophthalmol Vis Sci* 48: 1767–1772.
17. Ay I, Francis JW, Brown RH, Jr. (2008) VEGF increases blood–brain barrier permeability to Evans blue dye and tetanus toxin fragment C but not adeno-associated virus in ALS mice. *Brain Res* 1234:198–205.
18. Takata N, Hirase H (2008) Cortical layer 1 and layer 2/3 astrocytes exhibit distinct calcium dynamics in vivo. *PLoS ONE* 3:e2525.
19. Jobsis PD, Rothstein EC, Balaban RS (2007) Limited utility of acetoxymethyl (AM)-based intracellular delivery systems, in vivo: Interference by extracellular esterases. *J Microsc* 226:74–81.
20. Kerr JN, Greenberg D, Helmchen F (2005) Imaging input and output of neocortical networks in vivo. *Proc Natl Acad Sci USA* 102:14063–14068.
21. Takano T, et al. (2006) Astrocyte-mediated control of cerebral blood flow. *Nat Neurosci* 9:260–267.
22. Drew PJ, et al. (2010) Chronic optical access through a polished and reinforced thinned skull. *Nat Methods* 7:981–984.
23. Andresen V, et al. (2009) Infrared multiphoton microscopy: Subcellular-resolved deep tissue imaging. *Curr Opin Biotechnol* 20:54–62.
24. Nadal A, Fuentes E, Pastor J, McNaughton PA (1995) Plasma albumin is a potent trigger of calcium signals and DNA synthesis in astrocytes. *Proc Natl Acad Sci USA* 92: 1426–1430.
25. Vogel A, Venugopalan V (2003) Mechanisms of pulsed laser ablation of biological tissues. *Chem Rev* 103:577–644.
26. Ando J, Smith NI, Fujita K, Kawata S (2009) Photogeneration of membrane potential hyperpolarization and depolarization in non-excitable cells. *Eur Biophys J* 38:255–262.
27. Kreppel F, Kochanek S (2008) Modification of adenovirus gene transfer vectors with synthetic polymers: A scientific review and technical guide. *Mol Ther* 16:16–29.
28. Paques M, et al. (2007) High-resolution imaging of retinal cells in the living eye. *Eye (Lond)* 21(Suppl 1):S18–S20.
29. Isaka N, Padera TP, Hagendoorn J, Fukumura D, Jain RK (2004) Peritumor lymphatics induced by vascular endothelial growth factor-C exhibit abnormal function. *Cancer Res* 64:4400–4404.